Three-dimensional interconnected mesoporous anatase TiO$_2$ exhibiting unique photocatalytic performances

Weiyang Dong [a],[*], Youwei Yao [a], Li Li [a], Yaojun Sun [b], Weiming Hua [c], Guoshun Zhuang [a], Dongyuan Zhao [c], Shuwen Yan [a], Weihua Song [a]

[a] Department of Environmental Science and Engineering, Fudan University, 220 Handan Road, Shanghai, 200433, PR China
[b] Center for Analysis and Measurement, Fudan University, 220 Handan Road, Shanghai, 200433, PR China
[c] Department of Chemistry, Fudan University, 220 Handan Road, Shanghai, 200433, PR China

ABSTRACT

In this article, an ordered two-dimensional (2D) hexagonal mesoporous anatase crystals–silica nanocomposite was first synthesized using synchronous-assembly of surfactant and inorganic precursors molecules, and then a three-dimensional (3D) interconnected mesoporous anatase TiO$_2$ was prepared *via* an "extracting silica" approach. The results show that the mesopore channels in our titania are highly connected by plenty of 3D uniform intrawall mesopores while retaining mesostructural integrity and regularity. The TiO$_2$ prepared is completely anatase crystalline with uniform nanocrystals (13.0 nm in size) and a high specific surface area ($\sim$145 m^2/g). This method is mild, simple and can be easily repeatable. The photocatalytic degradation rates of Acid Red 1 (0.173 min^{-1}) and microcystin$-$LR (2.57 min^{-1}) on the interconnected mesoporous TiO$_2$ are very high, which are 41.6 and 2.85 times higher than that of the parent sample; 29.2 and 7.20 times that of P25 photocatalyst, respectively. These results clearly demonstrated that the 3D interconnected mesostructure played a key role in the activity increments. In addition, our photocatalysts are considerably stable and reusable. To the best of our knowledge, such results have not been seen in the literature before. Furthermore, the fundamentals of this study would provide new insights for the rational design and preparation of 3D highly interlinked mesoporous metal-oxides with unique photocatalytic performances.

© 2017 Elsevier B.V. All rights reserved.

1. Introduction

One of the most pervasive problems afflicting people over the world is inadequate access to clean water, and the water pollution problems are expected to grow worse in the coming decades [1]. More than 4 billion people globally are exposed to high levels of threat to water security [2,3], millions of people die annually (3900 children a day) from diseases transmitted through unsafe water [2]. Dyes and microcystins (MCs) are two major contamination sources of water bodies. About 1,000,000 tons of various dyes are annually produced worldwide [4,5], and over 400 tons of dyes per day are released into the environment during manufacturing, processing, using *etc.* [6–9]. The presence of dyes in water bodies has been recognized as one of the most important environmental hazardous substances, and the discharge of dyes from effluents is a matter of concern for both toxicological and esthetical reasons [10–12]. Azo dyes are the largest and the most important class of commercial dyes, accounting for *ca.* 70% of all commercial dyes [4,5,13–17], mainly due to their cost effectiveness, ease of synthesis, intense colouring properties *etc.* [18]. Most azo dyes are carcinogenic, harmful, and hard to be biodegraded due to their complex chemical structures and toxic breakdown products [19]. Among the azo dyes, acid red series is a primary member [20]. Acid red 1 (AR1, Fig. S1, Supplementary Material) has been classified as a non-biodegradable dye by the Environment Protection Agency [18,21], and there are evidences for the carcinogenic effect of its degradation products in anaerobic conditions [18]. Additionally, the existence of microcystins (MCs) in water is another major threat to human health. MCs, a family of potently cyclic heptapeptides hepatotoxins and tumor promoters, are the most common cyanotoxins produced by cyanobacterial harmful algal blooms occurring in eutrophic water such as lakes, ponds, reservoir and rivers, *etc.*, and are frequently responsible for poisoning animals and humans who come into contact with toxic blooms and contaminated water [22–24]. MCs are extremely toxic, and acute exposure to high levels

of which can result in lethal liver hemorrhage or liver failure [22]. A well-documented incident of MCs water contamination occurred in a hemodialysis clinic in Brazil in 1996, resulting in the deaths of over 50 patients [23,25]. Even chronic exposure to low levels of MCs would cause tumor promoting activity and it is possibly carcinogenic [22,26]. MCs possess more than 90 derivatives [27], of which microcystin−LR (MC−LR, 1.4 ∼ 2.9 nm [28], Fig. S1) is the most abundant and commonly detected, and also the most toxic isomer of MCs [22,29].

Conventional methods, such as coagulation, flocculation, sand filtration *etc.* have been used to deal with waters containing dyes or/and MCs. However, there are many shortcomings in these methods, such as the increasing number of refractory materials in effluents, the difficulties in the complete removal of color or/and dissolved MCs, and expensiveness [22,30]. Conventional biological treatment methods are often ineffective in decolorization and removal of azo dyes, due to a great degree of aromatics present in the molecules, their stability and biological persistence [9,31]. Moreover, the primary degradation products of azo dyes are generally aromatic amines, which are toxic, carcinogenic, and teratogenic [5,6]. Besides, biological methods require a long reaction time in treating MCs and are thus not viable [32,33]. The activated carbon adsorption is an effective means for the removal of dyes and MCs, however, it is an expensive method mainly due to the non-renewable use [22,30], and the deficiency of accessible mesopores for adsorption of large MCs [34].

During the past decades, many new methods (photocatalytic oxidations [13,23,24,26,27,33], photoelectrocatalytic oxidation [35], coupled photocatalytic oxidation and biofilm process [36], Fenton, photo-Fenton and photoelectro-Fenton processes [14–17,37], adsorption and fast separation of $Fe_3O_4@nSiO_2@mSiO_2$ core-shell structured microspheres [38], ultrasonically induced degradation [39], chemical oxidation such as ozonation and oxidation with hypochlorite ion [22,40], electrochemical and photoelectrochemical oxidation processes [18,40],) have been developed for removing the azo dyes or/and MCs worldwide, Among these approaches, photocatalytic oxidations, as emerging successful technologies, have attracted great attention due to their potential capability for complete degradation of organic molecules to mineralized end products, such as CO_2 and NH_3 [41,42]. Up to now, TiO_2 photocatalytic technology has been regarded to be the most efficient, environmentally benign and promising method, and numerous researches have been focused on it [13,23,26,27,43–48]. In this respect, ordered mesoporous TiO_2 has drawn particular interests because of its large mesopore size and high specific surface area [43,45,47–54].

It is well-known that 3D interconnected mesoporous network has the following remarkable advantages over 2D and 1D counterparts: (1) Considerably benefiting ingress/egress of guest species because of possessing far more openings to the internal porous networks at the surfaces; (2) Greatly enhancing diffusion efficiencies of guest molecules within the interconnected mesopore networks [55,56]; (3) Elevating both the accessibility and availability of the inner surfaces; (4) Allowing light to irradiate more inner surfaces through the openings and interlinked mesopore architectures, which can lead to an immense increment of •OH radical in number [55]; (5) Enhancing light harvesting efficiency due to the multiple scattering of light in the interpenetrated mesopores [57,58]. All of these prominent characteristics can significantly increase the photocatalytic oxidation performance. In addition, controlling the crystallinity, phase, and crystal size of the pore walls is also an important issue, because it determines their performances in practical applications [59,60]. For example, titania has three crystalline phases with the anatase polymorph showing the highest photocatalytic activity [45]. Both high crystallinity and large nanocrystals can obviously enhance activity [45,53]. However, so far there are

few reports on 3D mesoporous anatase TiO_2 with high interconnectivity, high crystallinity, large nanocrystals and big specific surface area for photocatalytically degrading azo dyes or/and MCs in the literature, because it is difficult to be prepared.

In this study, we first synthesized ordered 2D hexagonal mesoporous titania-silica nanocomposites using synchronous-assembly of surfactant and inorganic precursors molecules, then prepared a 3D interconnected mesoporous anatase TiO_2 *via* an "extracting silica" approach. The mesopore channels in our titania extracted are highly interpenetrated by the uniform intrawall mesopores, and the mesostructures are retained in the integrity and regularity, the TiO_2 is complete anatase crystalline with uniform nanocrystals in size (13.0 nm) and a much high specific surface area (∼ 145 m²/g). This method is simple, facile, and can be easily repeatable. AR1 and MC−LR were chosen as the target contaminants. The results indicated that our mesostructured TiO_2 with 3D interconnection presented very high photocatalytic degradation activities to AR1 and MC−LR, greatly higher than that of the parent sample and Degussa commercial P25 photocatalyst, in addition to being quite stable and reusable. The results have not been reported in the literature before. This approach is generally applicable to other ordered mesoporous metal oxides, such as niobium and tantalum oxides, *etc.*, opening up a new avenue to design and prepare 3D interconnected mesostructures with ultra-high photocatalytic performances, *etc.*

2. Experimental section

2.1. Chemicals

Titanium isopropoxide [Ti(OCH(CH$_3$)$_2$)$_4$, TIPO, ≥ 97%] and tetraethyl orthosilicate [Si(OC$_2$H$_5$)$_4$, TEOS, ≥ 96%] were purchased from Fluka. Pluronic P123 [M$_w$ = 5800, EO$_{20}$PO$_{70}$EO$_{20}$] was received from Aldrich. Ethanol (absolute), concentrated HCl (36.5 wt.%), NaOH (96%), HClO$_4$ (71%) were AR grade and purchased from Shanghai Chemical Corp. P25 photocatalyst (A commercial nano-crystalline TiO_2 consisting of *ca.* 80% anatase and 20% rutile; BET area *ca.* 50 m²g⁻¹) was kindly supplied by Degussa Corp. Acid Red 1 (AR1, C$_{18}$H$_{13}$N$_3$Na$_2$O$_8$S$_2$) bought from Sigma-Aldrich was prepared into 4.0×10^{-5} M solution with deionized water. Microcystin−LR (MC−LR) purchased from Agent Technology Co., Ltd and stored at −25 °C was prepared into 10 mg L⁻¹ (1.0×10^{-5} M) aqueous solution with Milli-Q water. Trifluoroacetic acid (TFA, 99.5 +%, HPLC grade) was purchased from Alfa Aesar. Acetonitrile (CH$_3$CN, ≥ 99.9% for HPLC) were purchased from Sigma-Aldrich Inc. All the chemicals were used as received without any further purification. The pH value of AR1 solution was adjusted to 2.0 by addition of diluted HClO$_4$ and NaOH solutions, in order to improve the adsorbability of mesoporous samples to AR1 (Fig. S2) and measured with PHS-3C meter, while the pH value of MC−LR solution was not adjusted and buffered.

2.2. Synthesis

The ordered 2D hexagonal mesoporous titania-silica nanocomposite (such as Ti/Si molar ratio = 80/20) was synthesized using TIPO as TiO_2 precursor, TEOS as SiO_2 precursor and P123 as a template according to the synchronous-assembly process of surfactant and inorganic precursors molecules [52]. The sample as-synthesized was calcined at 350 °C for 6 h in air to remove the organic template, subsequently crystallized at 900 °C for 2 h in air with a heating rate of 1 °C min⁻¹. Thus, the ordered 2D hexagonal mesoporous anatase TiO_2-SiO_2 nanocomposite was obtained and finely ground (parent sample), which was then treated with diluted NaOH solution (such as 0.5 M) at 40 °C according to a solid/liquid ratio of 1/10 (g mL⁻¹)

to extract silica [55]. The mixture in a sealed beaker was vigorously stirred for 12 h, and then the suspension was centrifuged to recover the solid. The solid was again impregnated in the newly taken 0.5 M NaOH solution using the same solid/liquid ratio as the above. This procedure was repeatedly progressed under the identical conditions for five more times. Finally, the product was thoroughly washed with deionized water under stirring, centrifuged, followed by dried at 100 °C for 24 h, then activated at 300 °C for 3 ∼ 6 h in air with a heating rate of 3 °C min^{-1}. The sample extracted was obtained.

2.3. Characterization

2.3.1. X-ray powder diffraction

Small-angle X-ray powder diffraction (SAXRD) patterns were recorded on a German Bruker D4 X-ray diffractometer with Ni-filtered Cu-Kα radiation (40 kV, 40 mA). Wide-angle X-ray diffraction (WAXRD) were collected on a Rigaku D/MAX-rB X-ray powder diffractometer using a high-power Cu-Kα (λ = 0.15418 nm) source operating at 40 kV and 60 mA with a graphite monochromator filter. The average size of anatase nanocrystals was estimated by using the Scherrer's equation to the half-height width of the 101 diffraction peak with silicon as a standard for the instrumental line broadening. The crystallinity of anatase nanocrystals was expressed with the intensity or area of the 101 diffraction peak.

2.3.2. Transmission electron microscopy (TEM)

TEM images were obtained on a JEM-2011 transmission electron microscope (JEOL Company) combined with energy dispersive X-ray spectroscopy (EDX) operating at 200 kV. For TEM measurements, the samples were prepared by sonication in ethanol and suspended on holey carbon grids. The contents of Ti and Si atoms in the samples were examined using energy dispersive X-ray spectroscopy (EDX).

2.3.3. N$_2$ adsorption-desorption isotherms

N$_2$ adsorption-desorption isotherms were collected on a Micromeritics ASAP 2010 Adsorption Analyzer at −196 °C (77 K). All samples were degassed at 250 °C for at least 5 h before analyses. The Brunauer-Emmett-Teller (BET) specific surface areas were calculated from adsorption data at a relative pressure range from 0.057 to 0.20. The total pore volumes (V$_T$) were calculated at a relative pressure of 0.976. Pore size distributions were calculated from adsorption branches using Barrett-Joyner-Halenda (BJH) method.

2.3.4. Adsorption and photocatalytic oxidation

Adsorption and photocatalytic oxidation of AR1 on the 3D interconnected mesoporous TiO$_2$ were investigated in air in a quartz vessel at room temperature according to our previous method [54,55]. 50 mL of dye aqueous solution and 50.0 mg of the catalyst powder finely ground were placed in the quartz vessel, which formed a suspension under stirring. For comparison, all the experiments were carried out under the identical conditions. The suspension was vigorously stirred first in dark for a certain time to evaluate the adsorption performance. After establishing adsorption-desorption equilibrium, UV light irradiation was turned on. The photocatalytic reaction was carried out under UV light irradiation from a 25 W low-pressure mercury lamp (λ = 254 nm). The radiant flux was measured with a photometer (International Light Model IL1400A). 1.0 mL of suspensions were taken at given time intervals and centrifuged at 15000 rpm for 15 min. The concentrations of dye were analyzed using a JASCO V–550 UV–vis spectrophotometer. For comparison, the performances of ordered 2D mesoporous titania-silica nanocomposite and P25 photocatalyst were also measured.

Adsorption and photocatalytic degradation of MC−LR were evaluated in air in a small quartz vessel at room temperature according to our previous method [54,55], using the same UV lamp and radiant flux as described above. 4.0 mL of 10 mg L^{-1} MC−LR solutions and 0.3 g L^{-1} of the sample powders finely ground were placed in the quartz vessel to form a suspension under vigorous stirring. Similarly, the suspensions were vigorously stirred first in dark for a certain time to assess the adsorption performance. After establishing adsorption-desorption equilibration, UV irradiation was turned on. 0.3 mL of suspensions were taken at timed intervals and centrifuged at 15000 rpm for 15 min. The supernatants were analyzed using high-performance liquid chromatography (HPLC) for the quantification of MC−LR. Separation and analysis were performed with an Agilent Series 1100 system equipped with a diode array detector (DAD) operated at 238 nm. An injection volume to a C18 column (5 μm, 4.6 × 250 mm, Agilent, USA) at 40 °C was 25 μL, and the HPLC was carried out under reverse phase condition referring to Ref. (23). The mobile phase in isocratic method with a flow rate of 1.0 mL min^{-1}, a mixture of 0.05% trifluoroacetic acid in water and 0.05% TFA in acetonitrile at a 60:40 ratio, was used to analyze the samples. MC−LR was eluted at about 6.9 min and measured with the DAD. The concentration change of MC−LR follows Lambert-Beer's law [54].

2.3.5. Stability and reusability

Stability and reusability were investigated by repetitively adsorbing and degrading AR1. After the dye was adsorbed and photocatalytically degraded each time, the sample was separated by centrifugation, followed by activating at 300 °C in air for 3 ∼ 6 h. Subsequently, it was re-used in the same concentration of AR1 solution.

3. Results and discussion

3.1. SAXRD and WAXRD

The SAXRD pattern of the mesoporous titania-silica nanocomposite (the parent sample) displays only one diffraction peak at 2 theta of 1.06° (Fig. 1Aa), which can be indexed as the 100 reflection of typical 2D hexagonal mesostructure (space group p6mm) [52], demonstrating an ordered arrangement of mesopore channels with a cell parameter (a_0) of 9.4 nm. For the sample extracted, the diffraction peak widens, but the peak position (2θ = 1.05°) and intensity have no obvious variation (Fig. 1Ab), indicating that the regularity of mesostructure retains intact by using our "mild extraction method".

The WAXRD pattern of the parent sample exhibits the characteristic diffraction peaks of anatase phase [52], and the intense narrow 101 peak (Fig. 1Ba). The area of the 101 diffraction peak is about 253 and the average size of the nanocrystals is calculated to be ∼ 12.5 nm, being larger than the cell parameter (9.4 nm). It implies that such sized nanocrystals may protrude into the cylindrical mesochannels and partially or fully block some channels. For the sample extracted, the intensity and area (254) of the 101 peak have no significant alterations (Fig. 1Bb), evidently illustrating that the crystals size and crystallinity are not essentially altered.

3.2. TEM observations

TEM images viewed along the [110] and [001] directions show that the parent sample (mesoporous TiO$_2$-SiO$_2$ nanocomposite) has an ordered 2D hexagonal straight mesopore channels without interconnection [Fig. 2(a-b)]. The cell parameter (a_0) is evaluated to be 9.9 nm, slightly larger than 9.4 nm calculated from the SAXRD patterns. The average size of the uniform mesochannels is measured to be 4.7 nm. HRTEM images further reveal that the
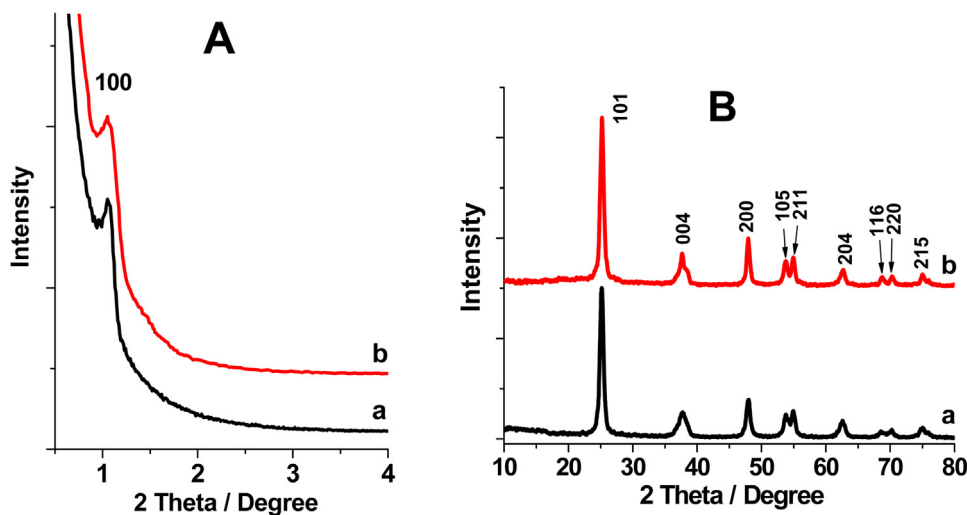
Fig. 1. SAXRD (A) and WAXRD (B) patterns of the mesoporous titania-silica nanocomposite (the parent sample) (a) and the sample extracted (b), respectively.

crystals are randomly oriented and link with the amorphous silica nanoparticles to form a "brick-mortar-like" framework structure. The majority of crystals overlap each other on the pore walls, while some crystals protrude into the mesochannels to produce ink-bottle-shape-like or blocked channels (marked with red square frames, Fig. 2b). The average size of nanocrystals is measured to be 13.1 nm, slightly larger than 12.5 nm calculated from the WAXRD patterns. The lattice fringes of the nanocrystals can be clearly observed and an average d-spacing is measured to be 0.34 nm, which is indexed as the 101 reflection of anatase structure, agreeing with the d_{101} spacing (0.35 nm) calculated from the WAXRD patterns. Here, the SiO_2 played a key role in restraining the transformation of anatase-to-rutile phase during the crystallization of the parent sample up to 900 °C [52,55].

Differently, the images along the [001] direction show many "peanut-shell-like" channel openings on the sample extracted [Fig. 2(c, e)]. The densely distributed intrawall pores can be clearly observed along the [110] direction [Fig. 2(d, f), some were marked]. Although the intrawall pores are random in orientations, they always link the mesochannels to form 3D hexagonal bimodal mesopore systems of high interconnection. The average size of the intrawall pores is measured to be 2.7 nm. The amorphous SiO_2 nanoparticles linking the anatase nanocrystals nearly completely disappear, leaving mesopores in the pore-walls. The HRTEM micrographs reveal that most mesochannels blocked are opened by the intrawall mesopores (areas marked in Fig. 2f), forming ink-bottle-shaped pores. Many of them are opened even by three or more intrawall mesopores (areas marked in Fig. 2f). Nevertheless, the mesostructures still retain their integrities and regularity. The average size of the mesochannels is measured to be 4.8 nm, essentially the same as that (4.7 nm) of the parent sample. The average size of anatase nanocrystals is measured to be 13.0 nm, essentially the same as that (13.1 nm) of the parent sample. The EDX analysis of the parent sample shows that the Ti/Si molar ratio is 80.6/19.4 (Fig. S3a), well agreeing with that (80/20) added in the synthesis sol. In the sample extracted, the Ti/Si atomic ratio is 98.3/1.7 (Fig. S3b). When the content of SiO_2 in the framework was lowered to 0.35%, the ordered mesostructures have collapsed (Fig. S4).

3.3. N_2 adsorption-desorption isotherms

The N_2 adsorption-desorption isotherms of the parent sample show typical type IV curve with one capillary condensation step in relative pressure (p/p_0) range of 0.46–0.64 (Fig. 3Aa), suggesting a narrow mesopore size distribution. The hysteresis loop displays H2 type, suggesting an ink-bottle-shaped mesopore geometry. This may be related to any mesochannel blockage from the protruding anatase nanocrystals [52], being in agreement with TEM observations (Fig. 2b). The mean pore size is about 4.4 nm (Fig. 3Ba), close to 4.7 nm evaluated from HRTEM observations. The BET specific surface area and pore volume calculated are 73 m^2g^{-1} and 0.08 cm^3g^{-1}, respectively.

It is of interest that the N_2 sorption isotherms of the sample extracted present two distinct uptakes on the sorption curve (Fig. 3Ab), which evidently suggests two sets of mesopores with varying size. The new minor N_2 uptake in low p/p_0 region (0.31–0.39) indicates the existence of a smaller mesopores possessing a narrow pore size distribution. The N_2 uptake in the p/p_0 region of 0.46–0.64 is markedly steeper than that of the parent sample, implying an increment of the mesopore channels, which probably come from the mesochannels opened. It is worth noted that the isotherms present unique and non-penetrated two hysteresis loops. The small loop in the p/p_0 region of 0.26–0.39 results from the intrawall mesopores. The drop of desorbed amount in the p/p_0 region of 0.39–0.48 is sharper than that of the parent sample, suggesting an increase of the ink-bottle-shaped mesopores, which should be ascribed to the mesochannels opened. The curve of pore size distribution exhibits two discrete and well-resolved peaks (Fig. 3Bb). The minor peak located at ca. 2.6 nm is narrow, clearly indicating the uniformity of the intrawall mesopore size. The mean size of mesochannels (ca. 4.5 nm) is almost the same as that of the parent sample. Both the BET specific surface area and pore volume (145 m^2g^{-1} and 0.156 cm^3g^{-1}) are almost two times that of the parent sample, respectively. These results evidently illustrate that the mesoporous structures have not collapse during our moderate SiO_2 extraction. All these results are well consistent with that from TEM and SAXRD measurements. To the best of our knowledge, the 3D highly interconnected mesoporous TiO_2 with large and uniform anatase nanocrystals, big specific surface area has not been observed in the mesoporous materials reported in the literature before.

3.4. Formation of 3D interconnected mesostructure

The ordered 2D hexagonal mesoporous titania-silica nanocomposites were first synthesized using the synchronous-assembly of surfactant and inorganic precursors molecules [52]. The samples as-synthesized have a uniform and homogeneous framework
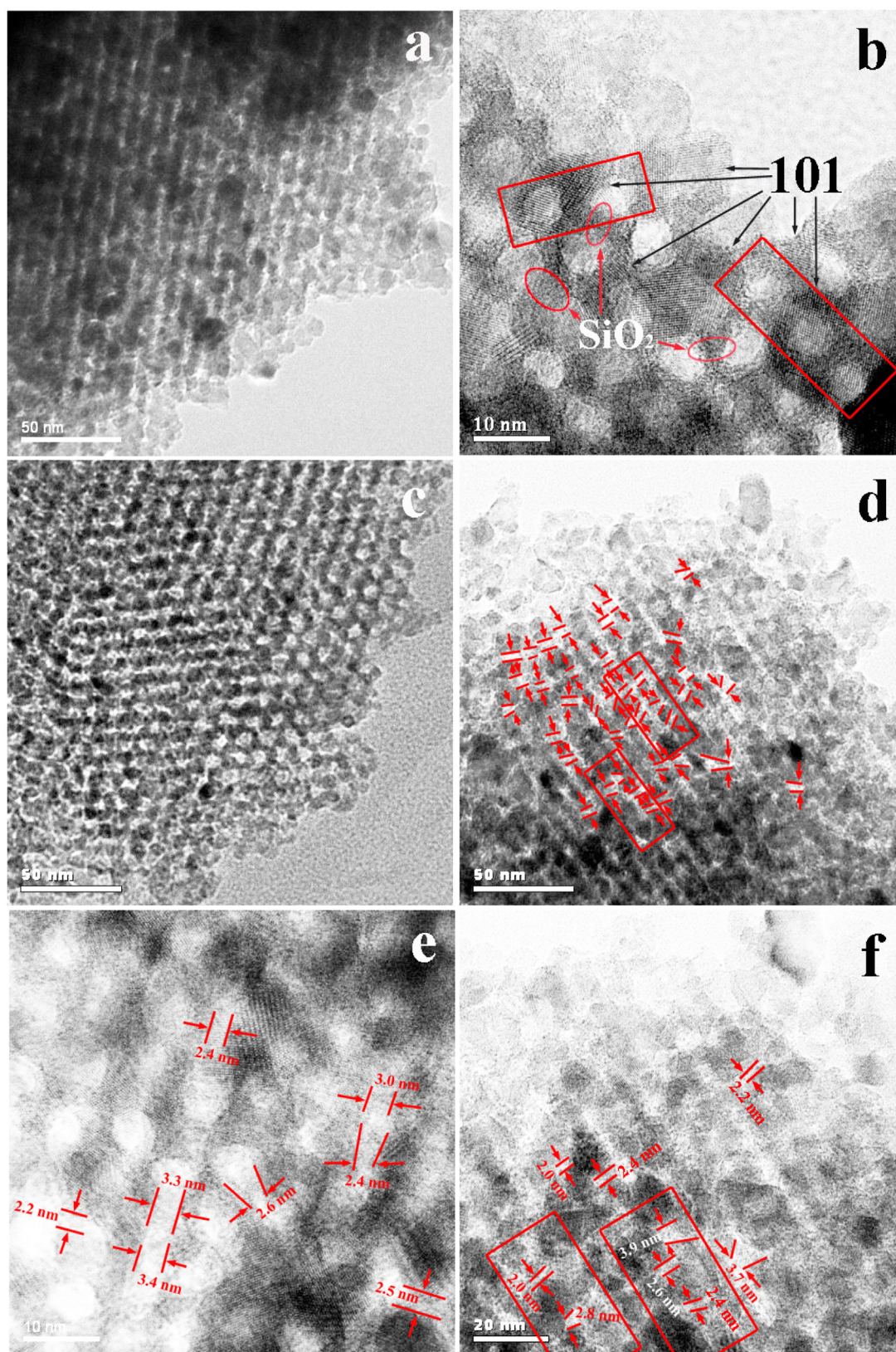
Fig. 2. Representative TEM (a, c, d) and HRTEM (b, e, f) images of the 2D hexagonal mesoporous TiO_2-SiO_2 nanocomposite (a–b) and the 3D interconnected mesoporous anatase titania (c–f), respectively; viewed along [110] (a, d, f) and [001] (b, c, e) directions.

with well-dispersed silicate. Upon calcination at 350 °C to remove the template molecules, the amorphous framework begins to crystallize. At this moment, phase separation occurs and anatase

nanocrystals are randomly embedded in the matrices of amorphous TiO_2 and SiO_2. The nanocrystals grow up with further increases of the temperature and/or time. Simultaneously, the amorphous
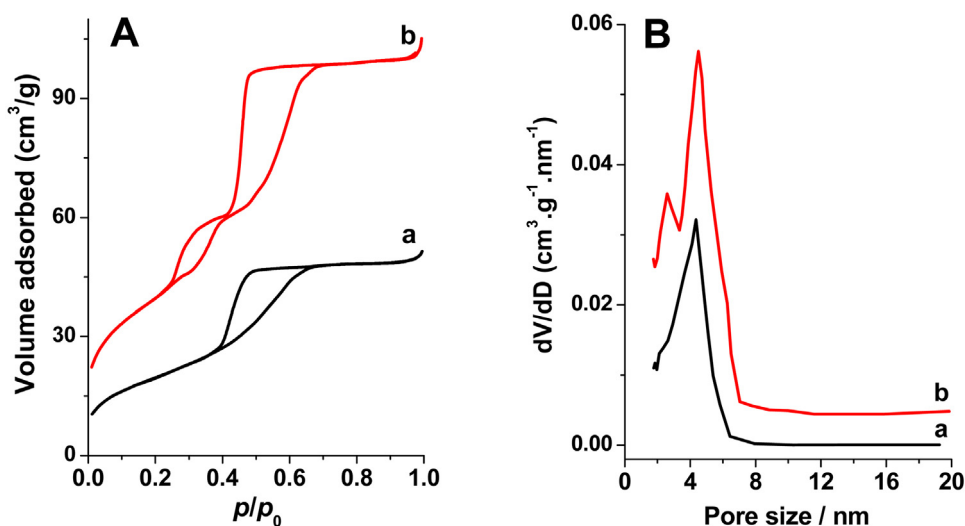
Fig. 3. N$_2$ adsorption-desorption isotherms (A) and pore size distributions (B) of the parent sample (2D mesoporous TiO$_2$-SiO$_2$ nanocomposite) (a) and the sample extracted (3D interconnected mesoporous TiO$_2$) (b), respectively.
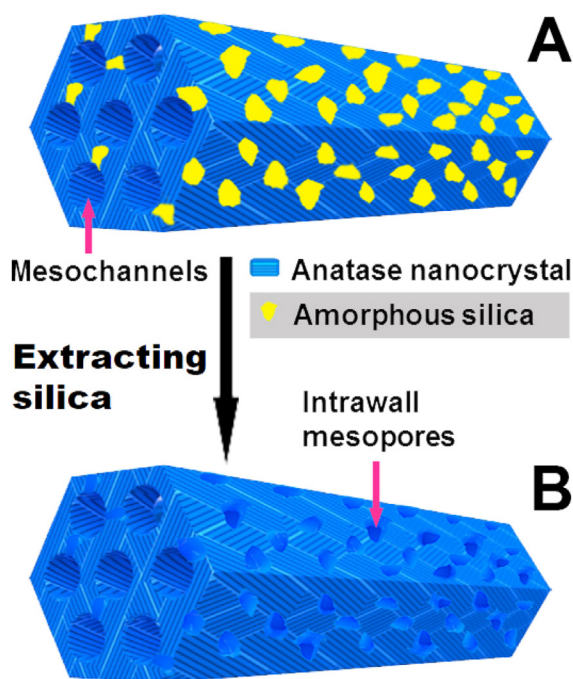

Fig. 4. Scheme for the formation of 3D interconnected mesoporous anatase TiO$_2$. (A), Ordered 2D hexagonal mesoporous anatase crystals-silica nanocomposite; (B), mesoporous anatase TiO$_2$ with 3D interconnection.

SiO$_2$ nanoparticles also enlarge, which serve as a glue linking the nanocrystals firmly together to form a unique "brick-mortar-like" framework. Additionally, the silica nanoparticles play a crucial role in stabilizing the mesopore structure and limiting the nanocrystals quickly coarsening. Therefore, we can readily obtain the ordered 2D hexagonal mesoporous anatase crystals-silica nanocomposites (Fig. 4A, parent sample) with full crystallization, large and uniform nanocrystals and silica nanoparticles (which is the decisive factor to yield mesoporous TiO$_2$ with 3D interconnection) by adjusting and controlling the temperature and time of crystallization, *etc.* Then, the 3D interpenetrated mesoporous anatase TiO$_2$ (Fig. 4B) was obtained using NaOH solution to extract silica from the parent sample obtained above. It needs to be pointed out that we use mild extracting method, by which the silica can be not only

extracted from the mesoporous framework, but the mesopore structural integrity and regularity, crystallinity and nanocrystals size can be retained intact as well. Accordingly, the photocatalytic performances of the materials prepared can be greatly enhanced.

3.5. Photocatalytic degradation of AR1

The adsorption of AR1 on the parent sample proceeds slowly, it takes *ca.* 22 min to essentially reach adsorption-desorption equilibration (Fig. 5Aa). The saturated adsorption amount is about 9.8%. As expected, the mesoporous TiO$_2$ with 3D interconnection displays considerably fast adsorption to AR1, the adsorption and desorption attain equilibrium in a quite short time ($\sim$3 min, Fig. 5Ac), which is *ca.* 7.3 times faster than that of the parent sample without intrawall mesopores and should be well ascribed to the contribution of the 3D interconnected mesochannels and networks. The enhancement of transport efficiency caused by the intrawall mesopores has also been observed in mesoporous silica SBA-15 [56]. Besides, the saturated adsorption amount for the 3D mesoporous sample (25.5%) is as high as 2.6 times that of the 2D parent sample, which have a negative correlation with the decrease of surface Si—OH groups in number (Fig. S5, Table S1), but have a positive correlation with the increases of surface areas and pore volumes. This is because that the adsorption of anionic dyes is predominantly driven by the surface Ti—OH groups [54]. On UV irradiation, the concentration of AR1 drops exponentially with photocatalytic degradation time on the parent sample, and the pseudo-first-order reaction is observed [Fig. 5(A, B)a]. The degradation rate is measured to be 0.00416 min^{-1}. Surprisingly, the 3D interpenetrated mesoporous TiO$_2$ exhibits a quite high activity to AR1 (0.173 min^{-1}) [Fig. 5Bc], which is up to 41.6 times that of the parent sample and 29.2 times that on commercial P25 photocatalyst (0.00593 min^{-1}), respectively. The alteration trend of activities (0.00416, 0.0487 [55], 0.173 min^{-1}) is not in complete accordance with the change of the number of total acids sites (30, 56 [55], 55) (Fig. S6, Table S1), indicating that the surface acid sites don't play the predominant role in the rate increase. These results demonstrate that the 3D highly interconnected mesoporous network of TiO$_2$ plays an overwhelming role in the tremendous increases of activity, while the large specific surface area and pore volume of the mesoporous TiO$_2$ also have a considerable contribution. In addition, the results of TOC analysis show that AR1 can be similarly mineralized in the photocatalytic process (Fig. S7). As expected, the mineralization
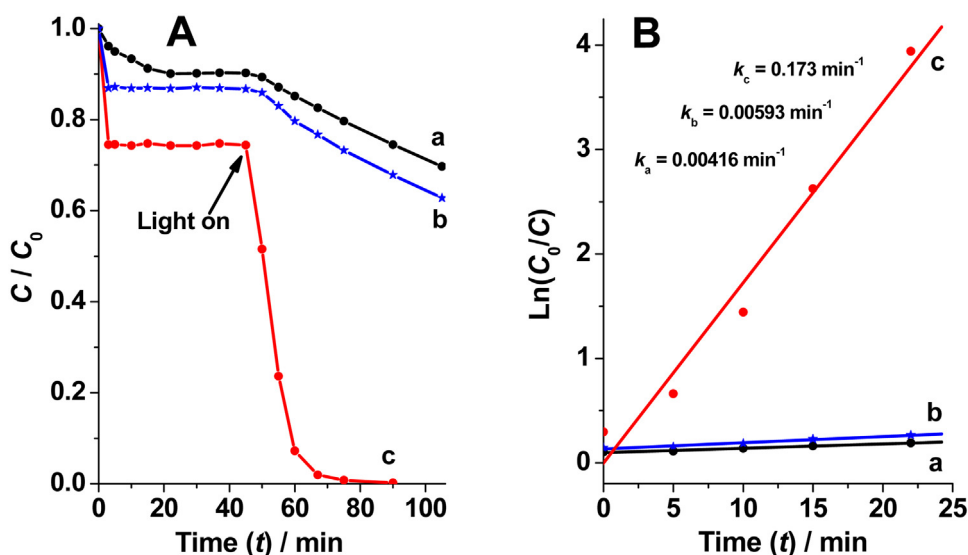
Fig. 5. (A), Adsorption and photocatalytic degradation of AR1 before and under UV light irradiation in the presence of samples, respectively. (B), Photocatalytic degradation rates of AR1 on the samples. (a) The parent sample (2D mesoporous TiO_2-SiO_2 nanocomposite), (b) Degussa P25 photocatalyst, (c) 3D interconnected mesoporous TiO_2 (the sample extracted).

efficiency of the 3D mesoporous anatase TiO_2 is far higher than that of the parent sample, and almost all the intermediates degraded are converted into CO_2 and H_2O *etc.* at the end of reaction.

3.6. Degradation of MC−LR

To make clear the performances of our samples displaying to bulkier molecules as well as different functional groups from azo dyes, MC−LR is chosen as a target contaminant. The time of adsorption reaching saturation is also very short ($\sim$5 min) on the 3D interconnected mesoporous TiO_2 and the saturated adsorption amount maintains no significant variation within 15 min, which is similar to the parent sample (Fig. 6A). Differently, the saturated adsorption amount on the TiO_2 with 3D interconnected mesopores ($\sim$28.4%) is higher than that on the 2D mesoporous TiO_2-SiO_2 nanocomposite ($\sim$22.9%). The amounts of MC−LR decline sharply with time under UV irradiation, and the rate follows pseudo-first-order (Fig. 6). Noteworthily, the 3D ordered mesoporous anatase TiO_2 displays a very high activity (2.57 min^{-1}), which is as high as 2.85 and 7.20 times that of the parent sample (0.903 min^{-1}) and P25 photocatalyst (0.357 min^{-1}), respectively.

3.7. Stability and reusability

Before UV light irradiation, the 3D mesoporous TiO_2 performs very fast adsorption to AR1, it takes only $\sim$3 min to essentially attain adsorption-desorption equilibration in the first cycle (Fig. 7a). The saturated adsorption amount is about 26.6%. After UV light irradiation, the concentration of AR1 declines exponentially with time and the degradation percentage is as high as 98.6% in 25 min. After fourteen more cycles [Fig. 7(b-o)], the equilibrium time is still *ca.* 3 min, while the saturated adsorption amount is in the range of 24.6∼28.4%, which has no significant change. All the degradation percentages are higher than 98.1%. Moreover, both the measurements of HRTEM and N_2 adsorption-desorption show that the mesostructure of the 3D mesoporous TiO_2 after using for fifteen cycles is essentially unvaried (Fig. S8). These results fully demonstrate that our sample with interconnected mesopores in 3D networks is quite stable and reusable.

3.8. Relationship of the photocatalytic activities with 3D interconnected mesostructure

In our 3D interconnected mesoporous TiO_2, the primary mesopore channels are highly interconnected by the intrawall mesopores in 3D manner and numerous pores open on the outer surfaces (Fig. 8), which benefit the guest molecules to diffuse into and out of, and greatly shorten the diffusion distances and times in the mesochannels, therefore the diffusion efficiency can be greatly improved. In addition, both the accessibility and availability of the surfaces in the depth of the mesochannels are tremendously increased, which can further enhance the performances of adsorption and photocatalytic degradation. Moreover, the large BET specific surface area and pore volume can provide more active sites of adsorption and photocatalysis, and accommodate more pollutant molecules, *etc.* The synergistic role of all these characteristics makes our anatase TiO_2 with mesochannels interconnection in 3D way generates very high activities to AR1 and MC–LR. The above results fully demonstrate that the architecture of 3D interconnected mesopores plays a key role in the tremendous increases of activities. Such results have not been seen in the literature till now.

3.9. Adsorption, diffusion and photocatalytic degradation processes

It is well known that the specific surface areas of the mesoporous photocatalysts come predominantly from the contributions of their inner surface areas. The anatase nanocrystals are documented to be dominantly inside the mesochannels due to the large inner surface, and the generation of •OH should occur dominantly on the inner surface, which deactivates rapidly and converts to an inactive surface −OH group in a near-diffusion-controlled rate [61]. Hence, •OH radicals scarcely diffuse out of the channels due to the very short diffusion distance (1.3−2.4 nm) inside the cylindrical mesopore channels. This clearly indicates that the photocatalytic reaction occurs predominantly inside the mesochannels. In addition, the dual-porous structure can more effectively promote light harvesting on the inner surface of the materials, and then enhance photocatalytic efficiency [62]. For our TiO_2 sample, the anatase nanocrystals exist predominantly inside the 3D interconnected mesochannels (Fig. 8). During reactions, the organic pollutant
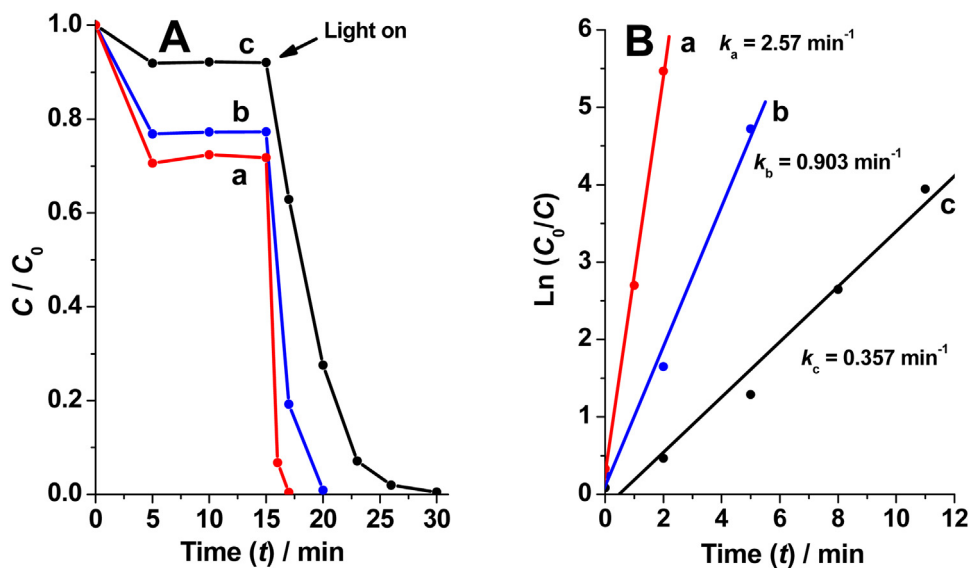
Fig. 6. (A), Adsorption and photocatalytic degradation of MC−LR before and under UV light irradiation in the presence of samples, respectively. (B), Photocatalytic degradation rates of MC−LR on the samples. (a) The 3D interconnected mesoporous TiO_2, (b) the parent sample (2D mesoporous TiO_2-SiO_2 nanocomposite), (c) Degussa P25 photocatalyst.
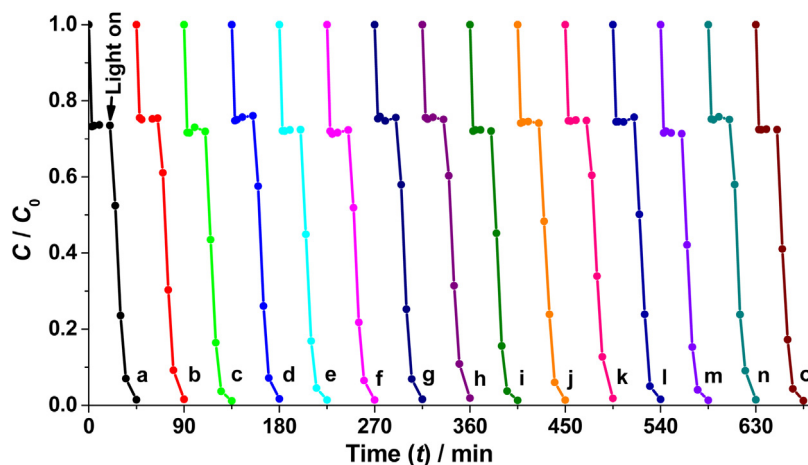

Fig. 7. Investigation of stability and reusability of the 3D interconnected mesoporous TiO_2 by repetitively adsorbing and degrading AR1. (a) to (o) are the first cycle to the fifteenth cycle, respectively.
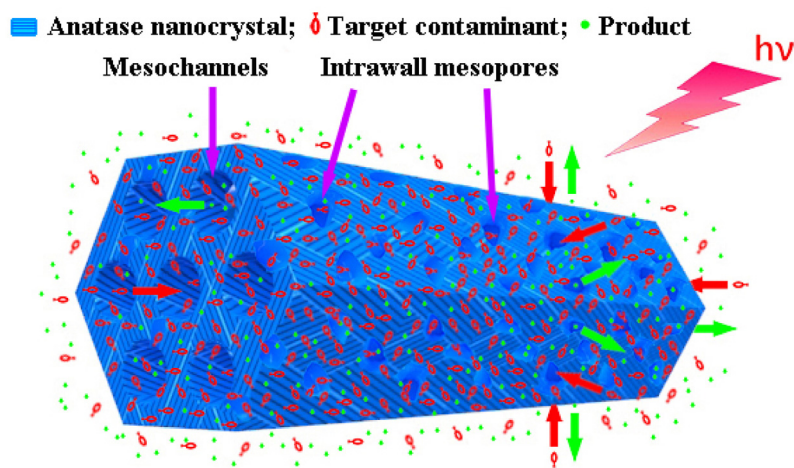

Fig. 8. Scheme for adsorption, diffusion and photocatalytic degradation processes of organic pollutants on the 3D interconnected mesoporous anatase TiO_2.

molecules are first adsorbed on the anatase nanocrystals on the outer surfaces. Subsequently, the molecules adsorbed diffuse inside the mesochannels in a rather short time through the numerous pore openings and interlinked mesopore network (Fig. 8). Meantime, the •OH radicals generated by the anatase nanocrystals under UV irradiation oxidize the molecules inside the interpenetrated mesopores. As a result, the molecules are in no time degraded into small pieces, and finally mineralized into CO_2, H_2O, etc (Fig. S7, S9). Then, CO_2, etc. could depart very easily from the reaction places inside the mesopores to the solution outside (Fig. 8). All these processes carry out very fast due to the 3D highly interconnected mesostructures and the high concentration of •OH radicals [55].

4. Conclusions

The 3D highly interconnected mesoporous TiO_2, with uniform anatase nanocrystals (13.0 nm in size) and a large specific surface area ($\sim$145 m^2/g), has been successfully prepared exploiting the approach of first synthesizing ordered 2D hexagonal mesoporous anatase crystals–silica nanocomposites and then extracting silica. This method is moderate, simple and can be facilely repeatable. The diffusion efficiency of AR1 in the 3D mesoporous TiO_2 is greatly enhanced, which is more than 7 times that in the parent sample without interlinked mesopores. The photocatalytic degradation rates of AR1 (0.173 min^{-1}) and MC−LR (2.57 min^{-1}) on the 3D mesoporous TiO_2 are quite high, which are 41.6 and 2.85 times higher than that of the parent sample; 29.2 and 7.20 times that of P25 photocatalyst, respectively. These results evidently indicate that the 3D mesoporous network of TiO_2 plays an overwhelming role in the increases of activities, while the large specific surface area and pore volume also have a considerable contribution. In addition, nearly all the intermediates degraded were converted into CO_2 and H_2O etc. at the end of reaction. It is very important that our photocatalysts are considerably stable and reusable. Up to now, such results have not been seen in the literature. Furthermore, this method would pave the way for the synthesis of ordered mesoporous other metal-oxides with 3D high interpenetration and unexpected performances, such as Nb_2O_5, Ta_2O_5, etc.

Notes

The authors declare no competing financial interest.

Acknowledgments

Appendix A. Supplementary data

Supplementary data associated with this article can be found, in the online version, at http://dx.doi.org/10.1016/j.apcatb.2017.05.083.

Characterization methods of ξ-potentials, FT-IR, TOC, LC-QTOF; molecular structures of AR1 and MC−LR; change curves of zeta potentials; EDX spectra; In-situ FT-IR spectra; data of surface acid sites; curves of TOC removal; TEM image; N_2 adsorption-desorption isotherms; results of ξ-potentials, FT-IR, TOC removal, LC-QTOF.

References

[1] M.A. Shannon, P.W. Bohn, M. Elimelech, J.G. Georgiadis, B.J. Mariñas, A.M. Mayes, Science and technology for water purification in the coming decades, Nature 452 (2008) 301–310.

[2] C.J. Vörösmarty, P.B. McIntyre, M.O. Gessner, D. Dudgeon, A. Prusevich, P. Green, S. Glidden, S.E. Bunn, C.A. Sullivan, C.R. Liermann, P.M. Davies, Global threats to human water security and river biodiversity, Nature 467 (2010) 555–561.

[3] S.B. Grant, J.-D. Saphores, D.L. Feldman, A.J. Hamilton, T.D. Fletcher, P.L.M. Cook, M. Stewardson, B.F. Sanders, L.A. Levin, R.F. Ambrose, A. Deletic, R. Brown, S.C. Jiang, D. Rosso, W.J. Cooper, I. Marusic, Taking the waste out of wastewater for human water security and ecosystem sustainability, Science 337 (2012) 681–686.

[4] S.Y. Yang, X. Yang, X.T. Shao, R. Niu, L.L. Wang, Activated carbon catalyzed persulfate oxidation of azo dye acid orange 7 at ambient temperature, J. Hazard. Mater. 186 (2011) 659–666.

[5] Y.F. Wang, D. Zhao, W.H. Ma, C.C. Chen, J.C. Zhao, Enhanced sonocatalytic degradation of azo dyes by Au/TiO2, Environ. Sci. Technol. 42 (2008) 6173–6178.

[6] S. Sekar, M. Surianarayanan, V. Ranganathan, D.R. MacFarlane, A.B. Mandal, Choline-based ionic liquids-enhanced biodegradation of azo dyes, Environ. Sci. Technol. 46 (2012) 4902–4908.

[7] P. Aravind, H. Selvaraj, S. Ferro, M. Sundaram, An integrated (electro- and bio-oxidation) approach for remediation of industrial wastewater containing azo-dyes: understanding the degradation mechanism and toxicity assessment, J. Hazard. Mater. 318 (2016) 203–215.

[8] C.P. Wang, Y.W. Zhang, L. Yu, Z.Y. Zhang, H.W. Sun, Oxidative degradation of azo dyes using tourmaline, J. Hazard. Mater. 260 (2013) 851–859.

[9] A. Safavi, S. Momeni, Highly efficient degradation of azo dyes by palladium/hydroxyapatite/Fe3O4 nanocatalyst, J. Hazard. Mater. 201 (2012) 125–131.

[10] K.S. Hu, X. Xiao, X.F. Cao, R. Hao, X.X. Zuo, X.J. Zhang, J.M. Nan, Adsorptive separation and photocatalytic degradation of methylene blue dye on titanate nanotube powders prepared by hydrothermal process using metal Ti particles as a precursor, J. Hazard. Mater. 192 (2011) 514–520.

[11] H. Métivier-Pignon, C. Faur-Brasquet, P.L. Cloirec, Adsorption of dyes onto activated carbon cloths: approach of adsorption mechanisms and coupling of ACC with ultrafiltration to treat coloured wastewaters, Sep. Purif. Technol. 31 (2003) 3–11.

[12] M. Rafatullah, O. Sulaiman, R. Hashim, A. Ahmad, Adsorption of methylene blue on low-cost adsorbents: a review, J. Hazard. Mater. 177 (2010) 70–80.

[13] C. Hu, X.X. Hu, L.S. Wang, J.H. Qu, A.M. Wang, Visible-light-induced photocatalytic degradation of azo dyes in aqueous AgI/TiO2 dispersion, Environ. Sci. Technol. 40 (2006) 7903–7907.

[14] C. Cai, Z.Y. Zhang, J. Liu, N. Shan, H. Zhang, D.D. Dionysiou, Visible light-assisted heterogeneous Fenton with ZnFe2O4 for the degradation of orange II in water, Appl. Catal. B: Environ. 182 (2016) 456–468.

[15] S. Garcia-Segura, E. Brillas, Combustion of textile monoazo, diazo and triazo dyes by solar photoelectro-Fenton: decolorization, kinetics and degradation routes, Appl. Catal. B: Environ. 181 (2016) 681–691.

[16] A.M.S. Solano, S. Garcia-Segura, C.A. Martínez-Huitle, E. Brillas, Degradation of acidic aqueous solutions of the diazo dye congo red by photo-assisted electrochemical processes based on Fenton's reaction chemistry, Appl. Catal. B: Environ. 168 (2015) 559–571.

[17] F.C. Moreira, S. Garcia-Segura, V.J.P. Vilar, R.A.R. Boaventura, E. Brillas, Decolorization and mineralization of sunset yellow FCF azo dye by anodic oxidation, electro-Fenton, UVA photoelectro-Fenton and solar photoelectro-Fenton processes, Appl. Catal. B: Environ. 142 (2013) 877–890.

[18] Md.M. Haque, W.T. Smith, D.K.Y. Wong, Conducting polypyrrole films as a potential tool for electrochemical treatment of azo dyes in textile wastewaters, J. Hazard. Mater. 283 (2015) 164–170.

[19] A.B. Dos Santos, F.J. Cervantes, J.B. Van Lier, Review paper on current technologies for decolourisation of textile wastewaters: perspectives for anaerobic biotechnology, Bioresour. Technol. 98 (2007) 2369–2385.

[20] R.S. Malani, S. Khanna, V.S. Moholkar, Sonoenzymatic decolourization of an azo dye employing immobilized horse radish peroxidase (HRP): a mechanistic study, J. Hazard. Mater. 256 (2013) 90–97.

[21] H.Y. Shu, C.R. Huang, M.C. Chang, Decolorization of mono-azo dyes in wastewater by advanced oxidation process: a case study of acid red 1 and acid yellow 23, Chemosphere 29 (1994) 2597–2607.

[22] T.P.J. Kull, P.H. Backlund, K.M. Karlsson, J.A.O. Meriluoto, Oxidation of the cyanobacterial hepatotoxin microcystin-LR by chlorine dioxide: reaction kinetics, characterization, and toxicity of reaction products, Environ. Sci. Technol. 38 (2004) 6025–6031.

[23] H. Choi, M.G. Antoniou, M. Pelaez, A.A. De la Cruz, J.A., Shoemaker, D.D. Dionysiou, Mesoporous nitrogen-doped TiO2 for the photocatalytic destruction of the cyanobacterial toxin microcystin-LR under visible light irradiation, Environ. Sci. Technol. 41 (2007) 7530–7535.

[24] M.G. Antoniou, J.A. Shoemaker, A.A. De la Cruz, D.D. Dionysiou, Unveiling new degradation intermediates/pathways from the photocatalytic degradation of microcystin-LR, Environ. Sci. Technol. 42 (2008) 8877–8883.

[25] S. Pouria, A. De-Andrade, J. Barbosa, R.L. Cavalcanti, V.T.S. Barreto, C.J. Ward, W. Preiser, G.K. Poon, G.H. Neild, G.A. Codd, Fatal microcystin intoxication in haemodialysis unit in Caruaru, Brazil, Lancet 352 (1998) 21–26.

[26] I. Liu, L.A. Lawton, D.W. Bahnemann, L. Liu, B. Proft, P.K.J. Robertson, The photocatalytic decomposition of microcystin-LR using selected titanium dioxide materials, Chemosphere 76 (2009) 549–553.

[27] M. Pelaez, P. Falaras, A.G. Kontos, A.A. De la Cruz, K. O'Shea, P.S.M. Dunlop, J.A. Byrne, D.D. Dionysiou, A comparative study on the removal of cylindrospermopsin and microcystins from water with NF-TiO2-P25

composite films with visible and UV–vis light photocatalytic activity, Appl. Catal. B: Environ. 121 (2012) 30–39.

[28] M. Sathishkumar, S. Pavagadhi, K. Vijayaraghavan, R. Balasubramanian, S.L. Ong, Experimental studies on removal of microcystin-LR by peat, J. Hazard. Mater. 184 (2010) 417–424.

[29] V.M. Vasconcelos, K. Sivonen, W.R. Evans, W.W. Carmichael, M. Namikoshi, Hepatotoxic microcystin diversity in cyanobacterial blooms collected in portuguese freshwaters, Water Res. 30 (1996) 2377–2384.

[30] S. Sansuk, S. Srijaranai, S. Srijaranai, A new approach for removing anionic organic dyes from wastewater based on electrostatically driven assembly, Environ. Sci. Technol. 50 (2016) 6477–6484.

[31] H.Y. Zhu, R. Jiang, L. Xiao, W.A. Li, A novel magnetically separable γ-Fe₂O₃/crosslinked chitosan adsorbent: preparation, characterization and adsorption application for removal of hazardous azo dye, J. Hazard. Mater. 179 (2010) 251–257.

[32] A.K.Y. Lam, P.M. Fedorak, E.E. Prepas, Biotransformation of the cyanobacterial hepatotoxin microcystin-LR, as determined by HPLC and protein phosphatase bioassay, Environ. Sci. Technol. 29 (1995) 242–246.

[33] P. Chen, L.Y. Zhu, S.H. Fang, C.Y. Wang, G.Q. Shan, Photocatalytic degradation efficiency and mechanism of microcystin-RR by mesoporous Bi_2WO_6 under near ultraviolet light, Environ. Sci. Technol. 46 (2012) 2345–2351.

[34] J. Lee, H.W. Walker, Effect of process variables and natural organic matter on removal of microcystin-LR by PAC-UF, Environ. Sci. Technol. 40 (2006) 7336–7342.

[35] S. Garcia-Segura, S. Dosta, J.M. Guilemany, E. Brillas, Solar photoelectrocatalytic degradation of Acid Orange 7 azo dye using a highly stable TiO_2 photoanode synthesized by atmospheric plasma spray, Appl. Catal. B: Environ. 132 (2013) 142–150.

[36] D.S. Kim, Y.S. Park, Comparison study of dyestuff wastewater treatment by the coupled photocatalytic oxidation and biofilm process, Chem. Eng. J. 139 (2008) 256–263.

[37] E.R. Bandala, D. Martinez, E. Martinez, D.D. Dionysiou, Degradation of microcystin-LR toxin by Fenton and photo-Fenton processes, Toxicon 43 (2004) 829–832.

[38] Y.H. Deng, D.W. Qi, C.H. Deng, X.M. Zhang, D.Y. Zhao, Superparamagnetic high-magnetization microspheres with an $Fe_3O_4@SiO_2$ core and perpendicularly aligned mesoporous SiO_2 shell for removal of microcystins, J. Am. Chem. Soc. 130 (2008) 28–29.

[39] W.H. Song, A.A. De la Cruz, K. Rein, K.E. O'Shea, Ultrasonically induced degradation of microcystin-LR and −RR: identification of products, effect of pH, formation and destruction of peroxides, Environ. Sci. Technol. 40 (2006) 3941–3946.

[40] C.A. Martı́nez-Huitle, E. Brillas, Decontamination of wastewaters containing synthetic organic dyes by electrochemical methods: a general review, Appl. Catal. B: Environ. 87 (2009) 105–145.

[41] K. Yu, S.G. Yang, C. Liu, H.Z. Chen, H. Li, C. Sun, S.A. Boyd, Degradation of organic dyes via bismuth silver oxide initiated direct oxidation coupled with sodium bismuthate based visible light photocatalysis, Environ. Sci. Technol. 46 (2012) 7318–7326.

[42] Z. Li, J.Y. Sheng, Y. Wang, Y.M. Xu, Enhanced photocatalytic activity and stability of alumina supported hematite for azo-dye degradation in aerated aqueous suspension, J. Hazard. Mater. 254 (2013) 18–25.

[43] J. Schneider, M. Matsuoka, M. Takeuchi, J.L. Zhang, Y. Horiuchi, M. Anpo, D.W. Bahnemann, Understanding TiO_2 photocatalysis: mechanisms and materials, Chem. Rev. 114 (2014) 9919–9986.

[44] K.Y. Lee, A. Mazare, P. Schmuki, One-dimensional titanium dioxide nanomaterials: nanotubes, Chem. Rev. 114 (2014) 9385–9454.

[45] X.B. Chen, S.S. Mao, Titanium dioxide nanomaterials: synthesis, properties, modifications, and applications, Chem. Rev. 107 (2007) 2891–2959.

[46] Y.Q. Qu, X.F. Duan, Progress, challenge and perspective of heterogeneous photocatalysts, Chem. Soc. Rev. 42 (2013) 2568–2580.

[47] P. Innocenzi, L. Malfatti, Mesoporous thin films: properties and applications, Chem. Soc. Rev. 42 (2013) 4198–4216.

[48] X. Li, J.G. Yu, M. Jaroniec, Hierarchical photocatalysts, Chem. Soc. Rev. 45 (2016) 2603–2636.

[49] P.D. Yang, D.Y. Zhao, D.I. Margolese, B.F. Chmelka, G.D. Stucky, Generalized syntheses of large-pore mesoporous metal oxides with semicrystalline frameworks, Nature 396 (1998) 152–155.

[50] B.C. Qiu, M.Y. Xing, J.L. Zhang, Mesoporous TiO_2 nanocrystals grown in situ on graphene aerogels for high photocatalysis and lithium-ion batteries, J. Am. Chem. Soc. 136 (2014) 5852–5855.

[51] W. Zhou, W. Li, J.Q. Wang, Y. Qu, Y. Yang, Y. Xie, K.F. Zhang, L. Wang, H.G. Fu, D.Y. Zhao, Ordered mesoporous black TiO_2 as highly efficient hydrogen evolution photocatalyst, J. Am. Chem. Soc. 136 (2014) 9280–9283.

[52] W.Y. Dong, Y.J. Sun, C.W. Lee, W.M. Hua, X.C. Lu, Y.F. Shi, S.C. Zhang, J.M. Chen, D.Y. Zhao, Controllable and repeatable synthesis of thermally stable anatase nanocrystal-silica composites with highly ordered hexagonal mesostructures, J. Am. Chem. Soc. 129 (2007) 13894–13904.

[53] W.Y. Dong, C.W. Lee, X.C. Lu, Y.J. Sun, W.M. Hua, G.S. Zhuang, S.C. Zhang, J.M. Chen, H.Q. Hou, D.Y. Zhao, Synchronous role of coupled adsorption and photocatalytic oxidation on ordered mesoporous anatase TiO_2-SiO_2 nanocomposites generating excellent degradation activity of RhB dye, Appl. Catal. B: Environ. 95 (2010) 197–207.

[54] W.Y. Dong, Y.J. Sun, Q.W. Ma, L. Zhu, W.M. Hua, X.C. Lu, G.S. Zhuang, S.C. Zhang, Z.G. Guo, D.Y. Zhao, Excellent photocatalytic degradation activities of ordered mesoporous anatase TiO_2–SiO_2 nanocomposites to various organic contaminants, J. Hazard. Mater. 229 (2012) 307–320.

[55] W.Y. Dong, Y.J. Sun, W.M. Hua, Y.W. Yao, G.S. Zhuang, X.C. Lv, Q.W. Ma, D.Y. Zhao, Preparation of secondary mesopores in mesoporous anatase-silica nanocomposites with unprecedented-high photocatalytic degradation performances, Adv. Funct. Mater. 26 (2016) 964–976.

[56] V.T. Hoang, Q.L. Huang, M. Eić, T.O. Do, S. Kaliaguine, Structure and diffusion characterization of SBA-15 materials, Langmuir 21 (2005) 2051–2057.

[57] Y.Z. Li, T. Kunitake, S. Fujikawa, Efficient fabrication and enhanced photocatalytic activities of 3D-ordered films of titania hollow spheres, J. Phys. Chem. B. 110 (2006) 13000–13004.

[58] H. Xie, Y.Z. Li, S.F. Jin, J.J. Han, X.J. Zhao, Efficient fabrication and enhanced photocatalytic activities of 3D-ordered films of titania hollow spheres, J. Phys. Chem. C. 114 (2010) 9706–9712.

[59] S.Y. Choi, B. Lee, D.B. Carew, M. Mamak, F.C. Peiris, S. Speakman, N. Chopra, G.A. Ozin, 3D hexagonal (R-3m) mesostructured nanocrystalline titania thin films: synthesis and characterization, Adv. Funct. Mater. 16 (2006) 1731–1738.

[60] M. Seo, S. Kim, J. Oh, S.-J. Kim, M.A. Hillmyer, Hierarchically porous polymers from hyper-cross-linked block polymer precursors, J. Am. Chem. Soc. 137 (2015) 600–603.

[61] Y. Shiraishi, N. Saito, T. Hirai, Adsorption-driven photocatalytic activity of mesoporous titanium dioxide, J. Am. Chem. Soc. 127 (2005) 12820–12822.

[62] X.C. Wang, J.C. Yu, C.M. Ho, Y.D. Hou, X.Z. Fu, Photocatalytic activity of a hierarchically macro/mesoporous titania, Langmuir 21 (2005) 2552–2559.